



Influence of the encapsulation degree of Fe⁰ active sites on performance of garnets for chemical looping partial oxidation of CH₄

Teng Zong^{a,b}, Lin Li^a, Yujia Han^{a,b}, Chaojie Wang^{a,b}, Yu Kang^c, Ming Tian^{a,*}, Chuande Huang^a, Xiaodong Wang^{a,*}

^a CAS Key Laboratory of Science and Technology on Applied Catalysis, Dalian Institute of Chemical Physics, Chinese Academy of Sciences, 457 Zhongshan Road, Dalian 116023, People's Republic of China

^b University of Chinese Academy of Sciences, 19(A) Yuquan Road, Shijingshan District, Beijing 100049, People's Republic of China

^c Max Planck Institute for Chemical Physics of Solids, Dresden, Germany

ARTICLE INFO

Keywords:

CH₄ conversion
Chemical looping
Garnet
Encapsulation of metals
Carbon resistance

ABSTRACT

It is of challenge to improve the coke resistance of Fe-based oxygen carriers (OC) due to the conflict of Fe⁰ sites for CH₄ activation but causing coke formation. The present work reported that carbon-tolerant of Y₃Fe₂Al₃O₁₂-T garnets (YFAO-T, T indicates calcination temperature) could be remarkably promoted by tuning calcination temperature for chemical looping partial oxidation of methane (CLPOM). This was because the encapsulation degree of Fe⁰ (1-Fe⁰_{exposed}/Fe⁰_{total}) became larger with reduction from 19% to 79% due to decreased oxygen mobility leading to more surface oxygen-deficiency for YFAO-T calcined at higher temperature, which not only resulted in Fe⁰ sites for CH₄ activation but also accessible lattice oxygen of garnet shell for carbon oxidation formed on Fe⁰ sites. Comparatively, the encapsulation of Fe⁰ was destroyed leading to progressively naked Fe⁰ with large particle size with reduction for YFAO-T calcined at lower temperature, which induced carbon deposition due to inaccessible lattice oxygen of garnets.

1. Introduction

Chemical looping partial oxidation of methane (CLPOM) is a promising approach to produce syngas with lower carbon footprint and energy consumption compared with conventional processes [1–7]. It includes two half reactions by using a metal oxide as oxygen carrier (OC). That is, CH₄ is partially oxidized by OC to generate syngas with ratio of H₂/CO of 2 suitable for the downstream applications such as methanol production and Fischer-Tropsch synthesis, and then the reduced OC is recovered by air. The process is exothermic thus avoiding energy input by combusting fossil energy which is entailed in conventional dry and steam reforming leading to large amount of carbon emission [8–13]. In addition, spatial separation of CH₄ and O₂ also prevents the risk of explosion without energy-intensive air separation unit to supply pure oxygen [10,14–17].

It is of great significance to develop OCs with high reactivity and selectivity as well as excellent anti-coke and redox stability for CLPOM. Fe-based OCs are the most studied for CLPOM thanks to its high oxygen storage capacity, low cost and environmental compatibility [18–23].

They usually exhibit different reactive behaviors due to their multiple oxidation state, and it is generally considered that deep reduction to metallic Fe is favorable for CH₄ conversion and CO formation but accompanied with carbon deposition due to CH₄ decomposition on Fe⁰ sites [18,24,25]. To this end, extensive efforts have been contributed to enhancing oxygen mobility to oxidize coke formed to CO. Tang et al. found that La and Ce modified catalysts were carbon-tolerant compared with Fe₂O₃/Al₂O₃, which could be attributed to lattice oxygen enhanced by synergistic La-Ce effect wherein both the LaFeO₃ and CeFeO₃ perovskites gave abundant oxygen defects facilitating lattice oxygen transfer kinetics [5]. Zhang et al. reported that the bulk oxygen mobility could be promoted by the enhancement of FeO₆ octahedral distortion in La_{1-x}Ce_xFeO₃, which accounted for La_{0.5}Ce_{0.5}FeO₃ with the highest FeO₆ distortion achieving exceptional syngas productivity of ~3 and 8 times higher than LaFeO₃ and CeFeO₃, respectively [26]. However, the enhancement of oxygen mobility was favorable for CO₂ formation in the initial of reaction thus the decrease in CO selectivity [27–29].

Recently, researchers attempt to construct the catalysts with core-shell structure to encapsulate Fe⁰ by selective metal oxides to improve

* Corresponding authors.

E-mail addresses: tm1982@dicp.ac.cn (M. Tian), xdwang@dicp.ac.cn (X. Wang).

<https://doi.org/10.1016/j.apcatb.2022.121421>

Received 21 January 2022; Received in revised form 12 April 2022; Accepted 14 April 2022

Available online 16 April 2022

0926-3373/© 2022 Elsevier B.V. All rights reserved.

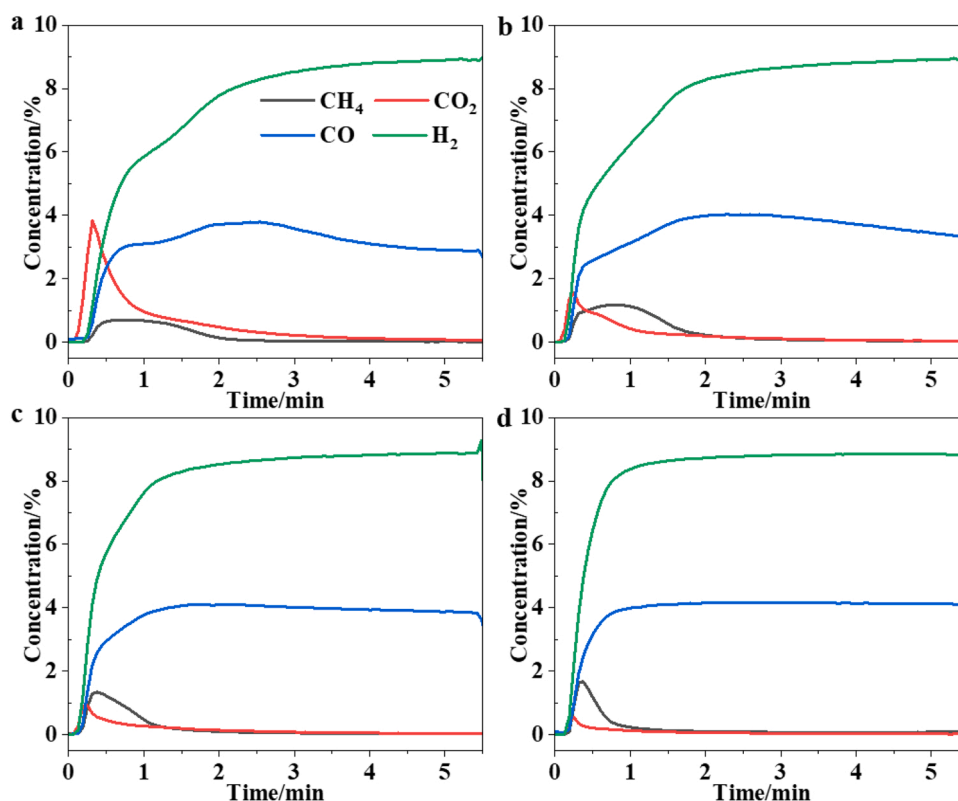


Fig. 1. Reaction kinetic curves of the fresh (a) YFAO-900, (b) YFAO-1000, (c) YFAO-1100, (d) YFAO-1200 for CLPOM.

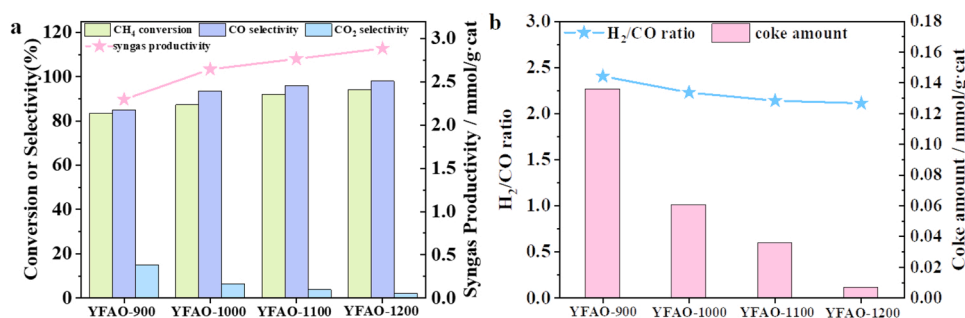


Fig. 2. (a) The conversion, selectivity, syngas productivity and (b) H_2/CO ratio, amount of coke of the YFAO-T OCs.

CO selectivity and carbon resistance. For example, Shafieifarhood et al. developed a core-shell $Fe_2O_3 @ La_xSr_{1-x}FeO_3$ OCs [30] which exhibited superior performance to $La_xSr_{1-x}FeO_3$ supported Fe_2O_3 counterparts in terms of activity, selectivity and carbon-resistance. This originated from the core-shell structure wherein nanoscale Fe_2O_3 cores provided more readily accessible lattice oxygen through the mixed conductive and selective shell and reduced the presence of metallic Fe on the surface leading to lower carbon formation [31]. Similar reactive behaviors were also reported for $Fe_2O_3 @ CeO_2$ with carbon deposition of only 28.7% of that for Fe-Ce composites, which could be attributed to rapid migration and supplement of oxygen ion preventing depletion of oxygen on the surface, and scarce Fe^0 on the surface due to the coverage of CeO_2 shell [32]. Besides fresh OCs with core-shell structure, our research group previously found that the encapsulation of Fe^0 by $LaSrFe_{1-x}Al_xO_4$ double perovskite occurred during CH_4 reduction, which avoided direct contact between CH_4 and Fe^0 thus preventing coke deposition [33]. Unfortunately, the OCs with core-shell structure usually exhibited unsatisfactory CH_4 conversion due to the covering of Fe^0 active sites and insufficient activation for CH_4 of the oxide shells. It is highly desired to tune the encapsulation of Fe^0 by more active oxide shells to achieve both

carbon resistance and CH_4 activation. Moreover, the evolution of the Fe-based OCs with core-shell structure during CH_4 reduction and their correlation with performance is not clear, which is of great value for the design of Fe-based OCs with high CH_4 conversion and CO selectivity concurrently without coke formation for CLPOM.

In our previous work, we for the first time demonstrated application of Fe-based garnets for CLPOM, [27] and found that Fe^0 in-situ formed was responsible for CH_4 activation [34]. In the present work, it was revealed that the encapsulation degree of Fe^0 by garnets ($1 - Fe_{exposed}^0 / Fe_{total}^0$, in which $Fe_{exposed}^0$ and Fe_{total}^0 were determined by CH_4 -TPSR and ^{57}Fe Mössbauer spectroscopy, respectively) could be tuned by oxygen mobility caused by the calcination temperature, which accounted for remarkably decreased carbon formation by almost 15 times concurrently with high CH_4 conversion and CO selectivity of $Y_3Fe_2Al_3O_{12}$ -T garnets (YFAO-T, T indicates calcination temperature) in CLPOM.

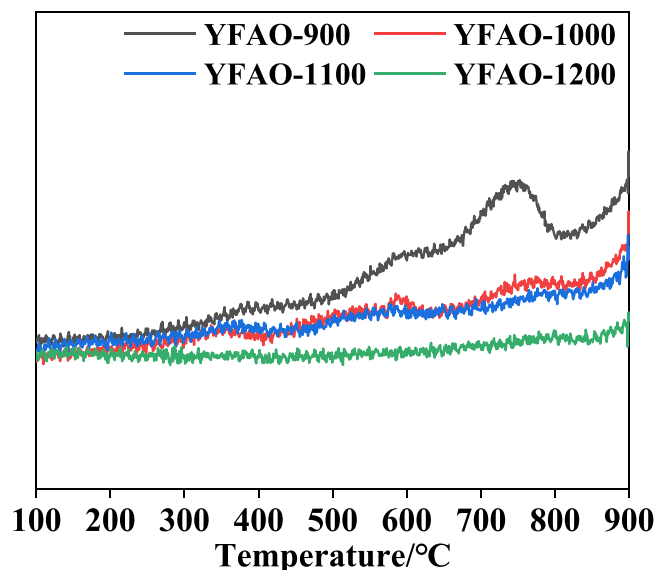


Fig. 3. The H_2 -TPR of the fresh YFAO-T samples.

2. Experimental

2.1. Preparation of OCs

The $Y_3Fe_2Al_3O_{12}$ garnets were synthesized by sol-gel method. Typically, $Y(NO_3)_3 \cdot 6H_2O$ (Aladdin, China), $Fe(NO_3)_3 \cdot 9H_2O$ (Aladdin, China), $Al(NO_3)_3 \cdot 9H_2O$ (Aladdin, China) with the corresponding stoichiometric ratio of garnet structure were dissolved in 200 mL deionized water. Then, citric acid and ethylene glycol were then added to the solution with the molar ratio of 2:1. The amount of the citric acid was 3 times of the total metal ions. After stirred for 1 h at room temperature to form a homogeneous solution, the resulting solution was put to 80 °C water bath under vigorous stirring to evaporate the water in solution and form the gel. After dried in an oven controlled at 120 °C overnight, the samples were calcined at different temperature (900 °C, 1000 °C, 1100 °C, 1200 °C) in air flow for 4 h (denoted as YFAO-T, T indicates calcination temperature).

2.2. Characterization of OCs

The crystal phases of the OCs were identified by PANalytical X'Pert-Pro powder X-ray diffractometer with $Cu K\alpha$ radiation of 0.1541 nm. The scanned 2θ range was 10–80° at 40 kV and 40 mA.

The high-resolution transmission electron microscopy (HRTEM) and

EDS element mappings were performed on JEM-2100 F instrument.

The ^{57}Fe Mössbauer spectra were conducted in a MFD-500AV-02 spectrometer working in the mode of constant accelerations, with ^{57}Co γ -quantum source constrained in Rh matrix. Around 10 mg cm^{-2} samples should be ensured during the test. The spectra were fitted via MossWinn software by using a least-squares fitting procedure. The isomer shifts (IS) were calibrated with respect to α -Fe at room temperature.

CH_4 -temperature programmed surface reaction (CH_4 -TPSR) was carried on the quartz fixed bed reactor using GAM200 quadrupole mass spectrometer (MS) to detect the outlet gas. 0.2 g samples was loaded into the quartz tube. After sweeping with helium, 5 vol% CH_4 balanced with He was flowed into the tube with the rate of 30 mL/min, and at the same time, the sample was heated from 30 °C to 900 °C at a ramping rate of 10 °C/min. H_2 -temperature programmed reduction (H_2 -TPR) experiment was basically the same as CH_4 -TPSR. The difference is the former using 0.1 g samples and 5 vol% H_2 in He (20 mL/min).

X-ray photoelectron spectroscopy (XPS) measurements were conducted on an ESCALAB 250 photoelectron spectrometer (Thermo Fisher Scientific, Al $K\alpha$, $h\nu = 1486.6$ eV) with a chamber pressure of 3×10^{-8} Pa to probe the state of the near-surface elements. All binding energies were calibrated with respect to the C 1s peak centered at 284.6 eV. Deconvolution of the peaks was processed with the XPSPEAK program using Shirley background subtraction and a mix of Gaussian-Lorentzian functions.

The in situ Raman spectra were conducted on a NanoWizard Raman spectroscope. YFAO-T-0.74, YFAO-T-1 samples were measured by a 532 nm laser source with the scanning range of 100–1868 cm^{-1} . Typically, a certain amount of samples were loaded into the in situ Raman cell. We implemented two experimental schemes. One is that the samples were heated from room temperature (RT) to 670 °C under 1 vol% CH_4 /Ar atmosphere with a heating rate of 10 °C/min. The spectra were recorded at RT, 470, 520, 570, 620, 670 °C. The other is that the samples were heated from RT to 500 °C under 1 vol% CH_4 /Ar atmosphere and then switched to the Ar further increasing temperature to 700 °C. The spectra were recorded at RT, 470, 500, 550, 600, 650, 700 °C.

2.3. Redox reactivity evaluation

A quartz fixed bed reactor was used for the reactivity test of OCs under atmospheric pressure. Typically, 0.2 g samples were loaded into the tube with an inner diameter of 6 mm. During the reduction step, 5 vol% CH_4 balanced with He was introduced into the reactor at a gas hourly space velocity (GHSV) of 6000 mL/g h^{-1} . For the oxidation step, 5 vol% O_2 in He was flowed into the tube with the rate of 30 mL/min. After each step, helium (30 mL/min) was used to sweep the line. The reaction took place at 900 °C. The outlet gas was detected and quantified by using GAM200 quadrupole mass spectrometer (MS). Before the

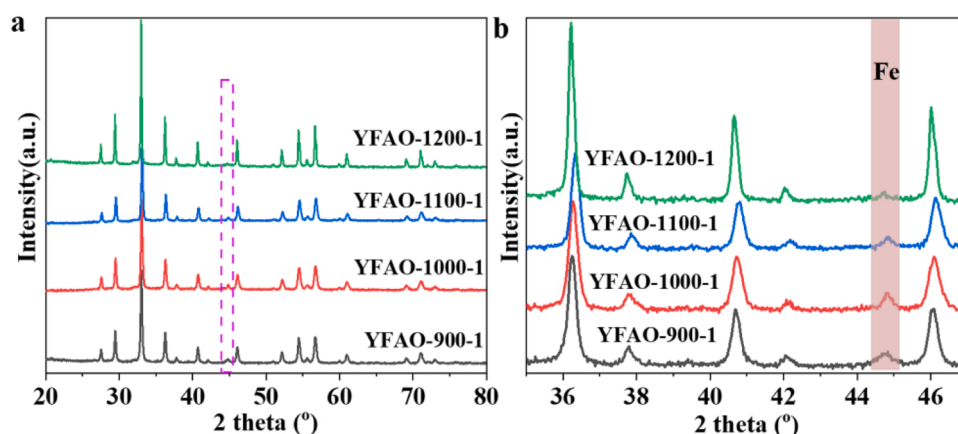


Fig. 4. X-ray diffraction patterns of YFAO-T-1.

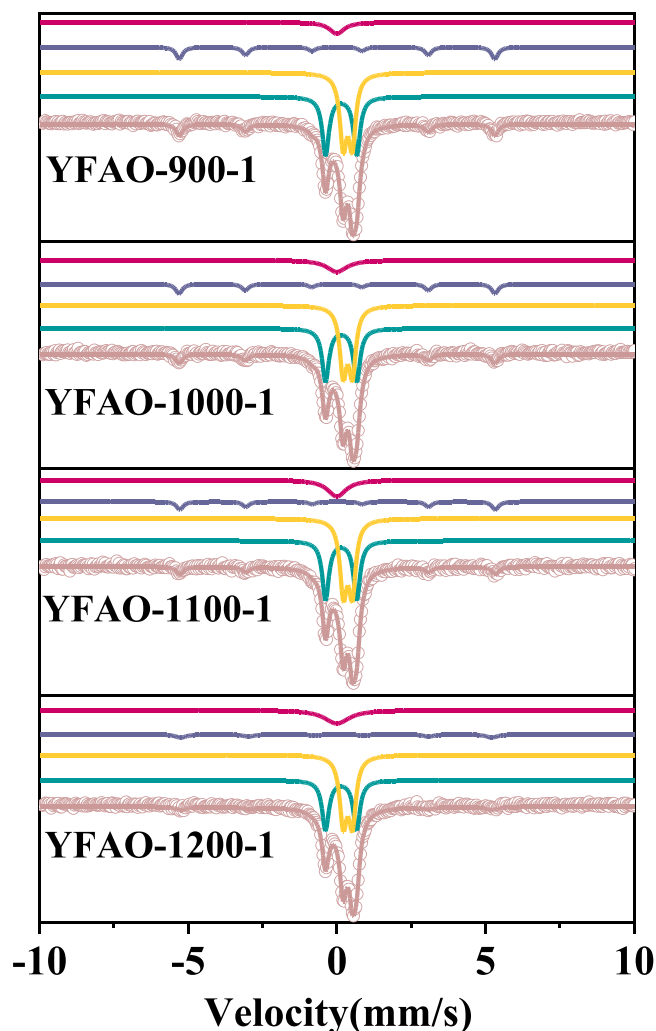


Fig. 5. $[^{57}\text{Fe}]$ Mössbauer spectra of YFAO-T-1.

measurement, the mass detector should be calibrated with various standard gas with known concentration. The amount of certain component is calculated by integrating the corresponding MS signals.

Table 1

The fitting parameters of ^{57}Fe Mössbauer spectra for the YFAO-T-1 samples.

Samples	IS (mm/s)	QS (mm/s)	H (T)	A (%)	Assignment	Actual oxygen converted (mmol/g) ^a	Fe ⁰ (mmol/g) ^b
YFAO-900-1	0.15	1.05		35.3	Fe ³⁺ (T)	0.99	0.66
	0.37	0.30		43.2	Fe ³⁺ (O)		
	0.00	0.01	33.0	13.8	α -Fe-L		
	0.00	–		7.7	α -Fe-S		
YFAO-1000-1	0.15	1.05		34.1	Fe ³⁺ (T)	1.05	0.70
	0.37	0.31		43.1	Fe ³⁺ (O)		
	0.00	0.01	33.0	11.6	α -Fe-L		
	0.00	–		11.2	α -Fe-S		
YFAO-1100-1	0.15	1.05		34.1	Fe ³⁺ (T)	1.04	0.69
	0.37	0.30		43.4	Fe ³⁺ (O)		
	0.02	0.01	33.0	9.0	α -Fe-L		
	0.00	–		13.6	α -Fe-S		
YFAO-1200-1	0.14	1.05		32.4	Fe ³⁺ (T)	1.04	0.69
	0.37	0.31		45.0	Fe ³⁺ (O)		
	0.02	-0.08	32.5	6.5	α -Fe-L		
	0.00	–		16.1	α -Fe-S		

$$^a \text{Actual oxygen converted} = \frac{30 \times A_{\text{Fe}^{0\%}}}{M_{\text{Y}_3\text{Fe}_2\text{Al}_3\text{O}_{12}}}$$

$$^b \text{Fe}^0 \text{ amount} = \frac{20 \times A_{\text{Fe}^{0\%}}}{M_{\text{Y}_3\text{Fe}_2\text{Al}_3\text{O}_{12}}}$$

The calculations of CH_4 conversion, CO selectivity, H/C ratio, syngas productivity and coke amount were given as followed.

$$X_{\text{CH}_4} = \frac{\int_0^t C_{\text{CO}_2, \text{out}} dt \times F + \int_0^t C_{\text{CO}, \text{out}} dt \times F}{\int_0^t C_{\text{CH}_4, \text{in}} dt \times F}$$

$$S_{\text{CO}}(\%) = \frac{\int_0^t C_{\text{CO}, \text{out}} dt \times F}{\int_0^t C_{\text{CO}_2, \text{out}} dt \times F + \int_0^t C_{\text{CO}, \text{out}} dt \times F}$$

$$\frac{H}{C} = \frac{\int_0^t C_{\text{H}_2, \text{out}} dt \times F}{\int_0^t C_{\text{CO}, \text{out}} dt \times F}$$

$$y_{\text{syngas}} = \frac{3 \times \int_0^t C_{\text{CO}, \text{out}} dt \times F}{V_m \times m_{\text{oxygen carrier}}}$$

Where F represents the gas flow rate in reduction step, C is the corresponding concentration in the gas in reduction step.

$$\text{Coke Amount} = \frac{(\int_0^t C_{\text{CO}_2, \text{out}} dt + \int_0^t C_{\text{CO}, \text{out}} dt) \times F_{\text{ox}}}{V_m \times m_{\text{oxygen carrier}}}$$

Where F_{ox} represents the gas flow rate in re-oxidation step, C is the corresponding concentration in the gas in re-oxidation step.

3. Results and discussion

3.1. The performance of YFAO-T

Fig. 1 shows kinetic curves of YFAO-T samples during reduction step of CLPOM. It could be seen that large amount of CO_2 formed at the beginning of reaction for YFAO-900 (Fig. 1a), which accounted for its CO selectivity of around 85% (Fig. 2a). Moreover, CO concentration reached the maximum at about 2 min and then decreased significantly, indicating that carbon deposition occurred and its amount accumulated to around 0.14 mmol/g (Fig. 2b). This explained that substantial amount of CO was detected in the initial stage of re-oxidation step caused by the oxidation of carbon species formed during reduction step (Fig. S1a). With the increase in calcination temperature, CO_2 concentration decreased remarkably and was negligible for YFAO-1200, which led to increase of CO selectivity to 98% (Fig. 2a). Furthermore, decrease of CO concentration was unobvious and hardly changed for several minutes in YFAO-1200 (Fig. 1d), indicating that coke formation declined (Fig. S1), which could be reflected by evidently decreased coke amount

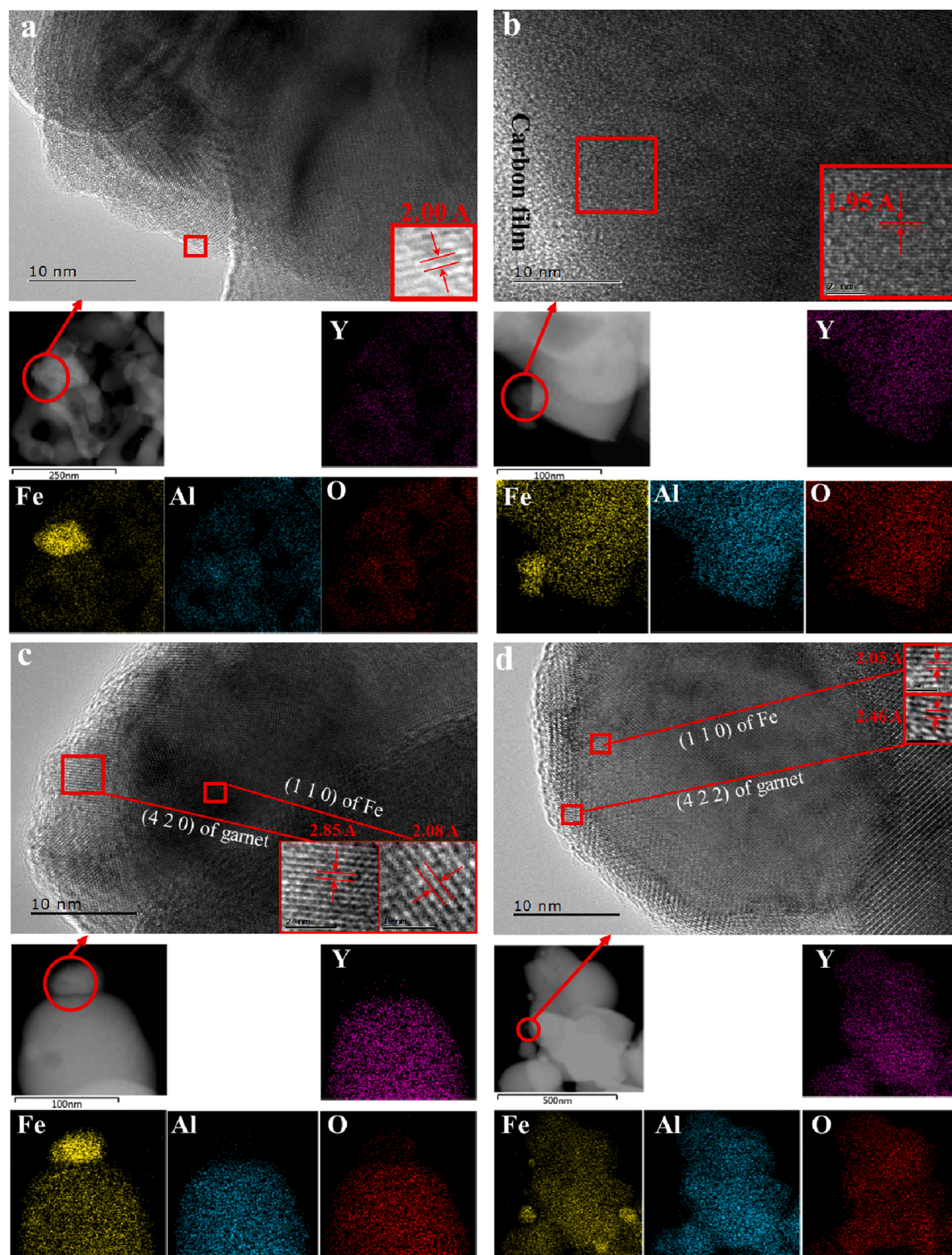


Fig. 6. HRTEM of (a) YFAO-900-1, (b)YFAO-1000-1, (c)YFAO-1100-1 and (d)YFAO-1200-1.

and H_2/CO ratio to about 2 (Fig. 2b). This resulted in significant increase of syngas productivity (Fig. 2a). The influence of calcination temperature on the performance of Fe-based perovskites and hexaaluminates has been reported. For example, Li et al. clarified that $\text{La}_{0.85}\text{MnFe}_{0.15}\text{O}_3$ and $\text{LaMn}_{0.9}\text{Fe}_{0.1}\text{O}_3$ perovskites calcined at 800 °C exhibited superior performance compared with those at 700, 750 and 850 °C due to higher oxygen mobility. Zhu et al. found that La-Fe-Al OCs calcined at 1100 °C showed the highest reactivity compared with those at 900, 1000 and

1200 °C thanks to compromising oxygen mobility and pure hexaaluminate phase [35,36]. In the present work, CO selectivity and anti-coke of YFAO-T samples enhanced with calcination temperature, indicating likely distinct mechanism of improvement which would be revealed in the following section.

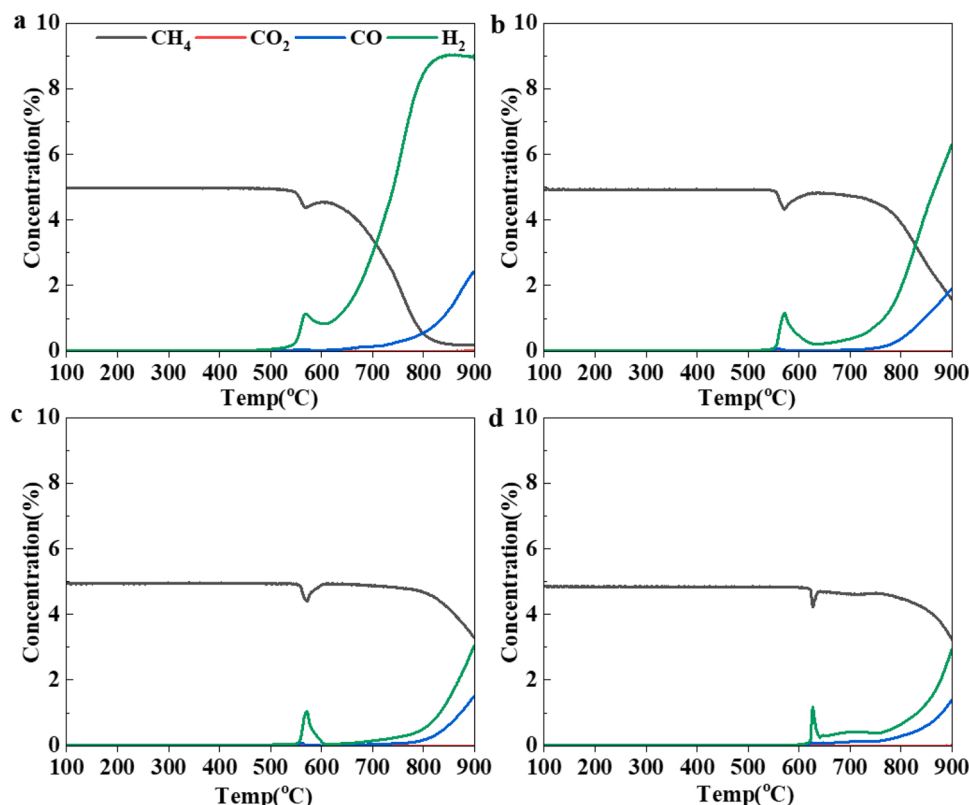


Fig. 7. CH₄-TPSR of (a) YFAO-900-1, (b) YFAO-1000-1, (c) YFAO-1100-1 and (d) YFAO-1200-1.

Table 2

The amount of H₂ produced by the decomposition of CH₄ on Fe⁰ site during CH₄-TPSR and the encapsulation degree of YFAO-T-O.

Samples	H ₂ amount (mmol/g)	Encapsulation degree (%)
YFAO-900-0.28	/	/
YFAO-1000-0.28	/	/
YFAO-1100-0.28	/	/
YFAO-1200-0.28	0.06	19 ^a
YFAO-900-0.74	0.19	4 ^a
YFAO-1000-0.74	0.198	6 ^a
YFAO-1100-0.74	0.159	22 ^a
YFAO-1200-0.74	0.08	60 ^a
YFAO-900-1	0.264	0
YFAO-1000-1	0.263	6 ^a
YFAO-1100-1	0.122	56 ^a
YFAO-1200-1	0.06	79 ^a

$$^a \text{ The encapsulation degree} = 1 - \frac{\text{Fe}_{\text{exposed}}^0}{\text{Fe}_{\text{total}}^0} = \left(1 - \frac{n_{\text{H}_2} \times n_{\text{Fe}_0}/0.264}{\text{Fe}_{\text{total}}^0}\right) \times 100\%,$$

in which n_{Fe_0} and 0.264 represented the amount of Fe⁰ (determined by ⁵⁷Fe Mössbauer spectroscopy listed in Table 1) and H₂ of YFAO-900-1, and $\text{Fe}_{\text{total}}^0$ and n_{H_2} represented that of the corresponding samples. In addition, we assumed that CH₄ decomposition only occurred on Fe⁰ and its rate on every exposed metallic iron site was constant, and the influence of carbon deposition on CH₄ decomposition over Fe⁰ was not considered.

3.2. The characterization of fresh YFAO-T

X-ray diffraction patterns of fresh YFAO-T samples was shown in Fig. S2. Only peaks attributed to garnet phase could be observed in all the four samples without those of iron oxide, indicating that calcination at 900 °C to 1200 °C could lead to formation of garnet phase and Fe species completely entered into garnet structure for YFAO-T samples. This could be further confirmed by the results of EDX mapping of fresh

YFAO-T samples wherein Y, Fe, Al and O elements were distributed evenly without Fe₂O₃ aggregation (Fig. S3). Mössbauer spectra of fresh YFAO-T samples is shown in Fig. S4 and corresponding fitting parameters are listed in Table S1. Two doublets were observed in all the four samples with IS of about 0.15 mm/s and 0.36 mm/s, and QS of 1.05 mm/s and 0.33 mm/s, which could be attributed to Fe³⁺ in tetrahedral and octahedral Al sites, [27,34] respectively, and their amount hardly changed with increase in calcination temperature. These results indicated that calcination at all the four temperature led to the formation of garnet phase and Fe³⁺ entered into tetrahedral and octahedral Al sites with similar amount. The results of H₂-TPR for YFAO-T samples are shown in Fig. 3. It could be seen that a peak of H₂ consumption at around 750 °C for YFAO-900 was observed but it decreased obviously with increase in calcination temperature and could be hardly detected for YFAO-1200, indicating that Fe-O bond strength enhanced, e.g. reactivity of lattice oxygen decreased. In addition, Fig. S5 showed that CO concentration at relatively lower temperature range (700–750 °C) decreased remarkably with increase of calcination temperature, which also confirmed declined reactivity of lattice oxygen of garnet. Fig. S6 depicted the amount of lattice oxygen converted of YFAO-T as a function of reaction time and it could be seen that the amount and rate of oxygen released during reaction time of about 3 min was always lower for YFAO-T calcined at higher temperature than that for those calcined at lower temperature, which should be due to slower oxygen diffusion in the bulk leading to deficiency of surface oxygen thus decreased oxygen conversion. Such the decline in the reactivity of lattice oxygen should account for decreased CO₂ formation in the initial of reduction step thus the increase in CO selectivity since highly active oxygen species were considered to be facile to CH₄ combustion [12,37,38].

3.3. The characterization of reduced YFAO-T-O

Our previous results presented that Fe⁰ formed in the initial of the reduction process for Fe-based garnets was active sites for CLPOM.

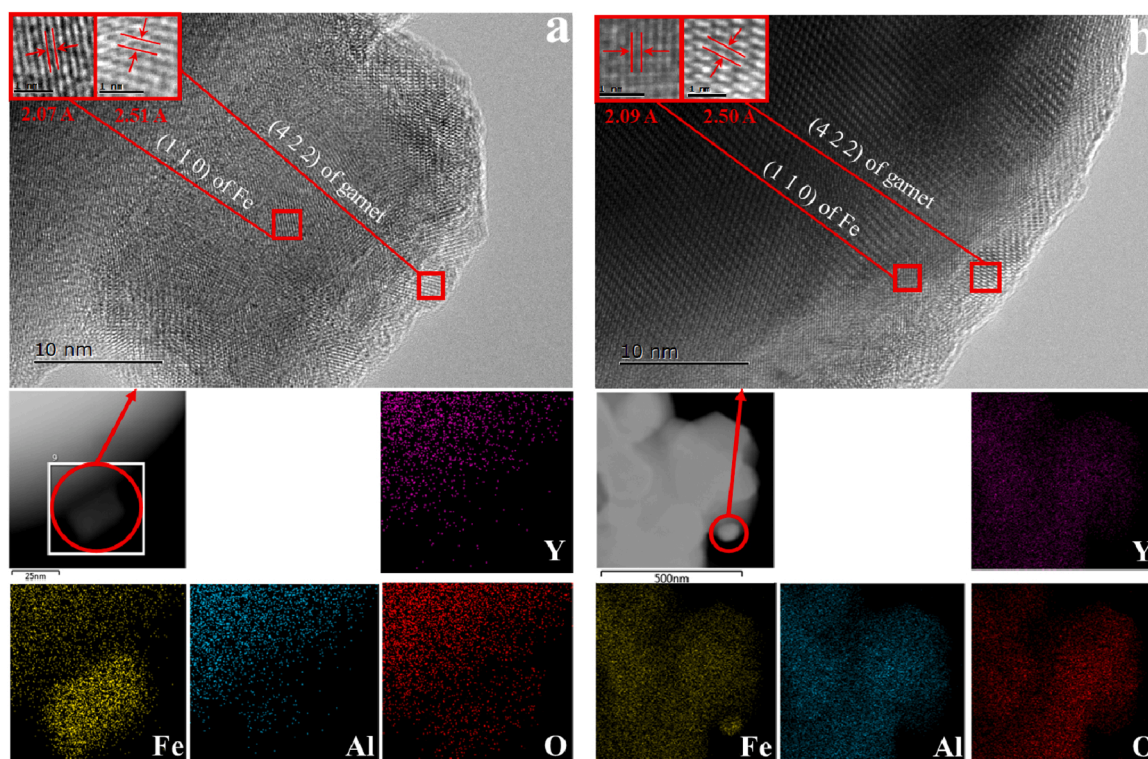


Fig. 8. HRTEM of (a) YFAO-1100-0.28 and (b) YFAO-1200-0.28.

Consequently, the characterization of OCs after CH₄ reduction with similar amount of oxygen converted of about 1 mmol/g (YFAO-T-O, O indicates amount of oxygen converted) was carried out to investigate the influence of calcination temperature on the chemical state of Fe⁰. Fig. 4 shows X-ray diffraction patterns of YFAO-T-1. The peaks of Fe⁰ were observed for all the four reduced samples and its intensity decreased with the increase in calcination temperature, indicating likely declined crystal size of Fe⁰. ⁵⁷Fe Mössbauer spectra of these four samples was shown in Fig. 5 and the corresponding fitting parameters were listed in Table 1. It could be seen for YFAO-900-1 that one new sextet (IS=0 mm/s, H=33 T) and singlet (IS=0 mm/s) were also identified besides those attributed to Fe³⁺ in tetrahedral and octahedral Al sites of garnet, which should be ascribed to magnetic and superparamagnetic α -Fe species with large and small crystal size (denoted as α -Fe-L and α -Fe-S), respectively [34,38], and their amount was 13.8% and 7.7%. These two sub-spectra could be still detected with the increase

in the calcination temperature but their amount changed a lot. Specifically, the amount of α -Fe-L decreased to 6.5% while that of α -Fe-S increased to 16.1% for YFAO-1200-1, which suggested that the crystal size of Fe⁰ declined with the increase of calcination temperature, in line with XRD results (Fig. 4). This could be further supported by EDX characterization of these four samples wherein aggregated Fe⁰ was prominent for YFAO-900-1 and they became smaller with the increase in calcination temperature (Fig. S7). HRTEM results of these four samples are shown in Fig. 6. For YFAO-900-1 and YFAO-1000-1, naked Fe⁰ with the lattice fringe spacing of about 2 Å ascribed to (110) plane could be seen on garnet (Fig. 6a, b). Different from these two samples, a layer with the lattice fringe spacing of about 2.8 Å was observed around Fe⁰ particles for YFAO-1100-1 (Fig. 6c), which should be ascribed to (420) plane of garnet, indicating that the increase in calcination temperature led to the encapsulation of Fe⁰ by garnet. This could be seen more clearly for YFAO-1200-1 in which Fe⁰ particles were covered by an overlayer of garnet (Fig. 6d), which explained why the particle size of Fe⁰ decreased with the increase in calcination temperature (Fig. 4, 5 and Fig. S7). Considering that chemical looping is a dynamic process consisting of not

only many reduction but also re-oxidization steps, the characterization of YFAO-1200-1 after 5th reduction and re-oxidization was carried out to study the effect of multiple redox cycles on the encapsulation. XRD and EDX mapping results of YFAO-1200-1 after re-oxidization (YFAO-1200-1-Re) showed that only garnet phase was observed without Fe⁰ (Fig. S8), and Y, Fe, Al and O elements evenly distributed (Fig. S9), indicating that the encapsulation of Fe⁰ disappeared and garnet structure recovered after re-oxidization. In addition, HRTEM result of YFAO-1200-1 after 5th reduction presented that Fe⁰ was still encapsulated by garnet after reduction of multiple redox cycles (Fig. S10), suggesting that the garnet overlayers could re-form after subsequent reduction despite its disappearance after re-oxidization during redox cycles. In order to study the encapsulation degree ($1 - \text{Fe}_{\text{exposed}}^0 / \text{Fe}_{\text{total}}^0$), CH₄-TPSR of these four samples was carried out and the results are shown in Fig. 7. H₂ without CO was detected accompanied by CH₄ consumption at around 600 °C for all the four samples, indicating that CH₄ decomposition occurred on Fe⁰ sites, and Fe⁰ was partially rather than completely encapsulated by garnet for YFAO-1100-1 and YFAO-1200-1. Otherwise, H₂ and CO formation should be concurrently observed as shown in CH₄-TPSR of fresh garnets without Fe⁰ sites (Fig. S5). It should be noted that H₂ amount remarkably decreased with the increase in calcination temperature and that for YFAO-1200-1 was almost five times lower than that for YFAO-900-1 (Table 2), indicating that the encapsulation degree of Fe⁰ enhanced with the calcination temperature. Considering that Fe⁰ was naked for YFAO-900-1 (Fig. 6), the encapsulation degree of Fe⁰ for the other three samples could be calculated based on their corresponding amount of Fe⁰ (Table 1) and H₂ (Table 2) referenced to those of YFAO-900-1 with the assumption of CH₄ decomposition only occurring on Fe⁰ and its rate on every exposed metallic iron site being constant and without considering the influence of carbon deposition on CH₄ decomposition over Fe⁰, and they were 6%, 56% and 79%, respectively (Table 2). Such different encapsulation degree for YFAO-T with the variation of calcination temperature might be related to oxygen mobility (Fig. 3 and Fig. S5).

The encapsulation of metals by reducible oxides has been identified

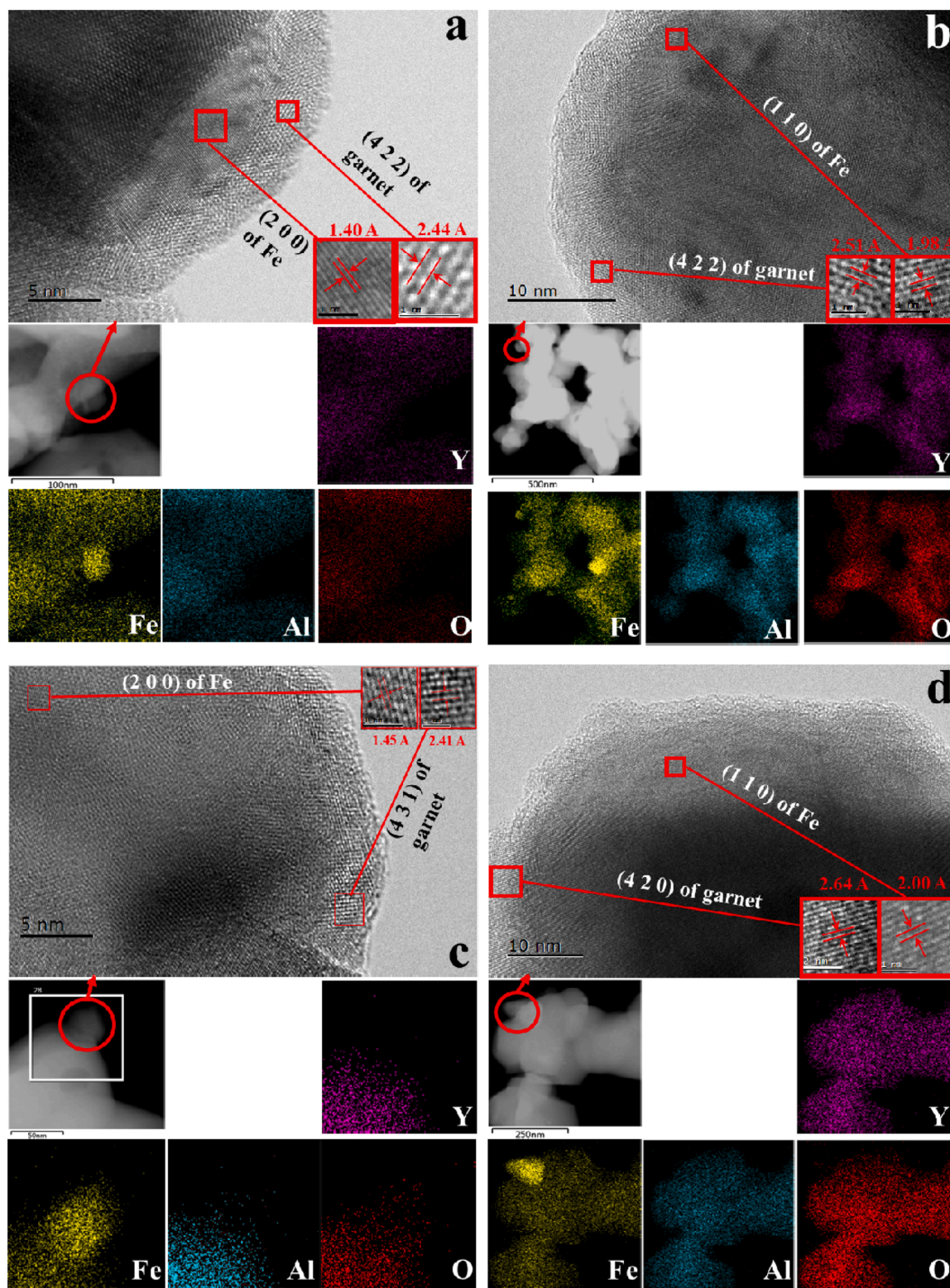


Fig. 9. HRTEM of (a)YFAO-900–0.74, (b)YFAO-1000–0.74, (c)YFAO-1100–0.74 and (d)YFAO-1200–0.74.

in various systems such as CeO_2 , TiO_2 and perovskites supported noble and transition metals [39–43]. To the best of our knowledge, the encapsulation of metals by garnets has not been reported. In order to investigate the influence of calcination temperature on the encapsulation of Fe^0 by garnets, the characterization of samples after reduction for different time was carried out, namely YFAO-T-0.28 and YFAO-T-0.74. XRD of YFAO-T-0.28 showed that the intensity of Fe^0 peaks for all the

samples was relatively low (Fig. S11), indicating that their amount was small, which could be supported by ^{57}Fe Mössbauer spectra of YFAO-T-0.28 wherein the amount of Fe^0 was about 1 wt% and only $\alpha\text{-Fe-S}$ was observed (Fig. S12 and Table S2). EDX results of YFAO-T-0.28 presented that Fe elements distributed evenly with Y, Al and O without Fe aggregates for YFAO-900–0.28 and YFAO-1000–0.28 whereas quite small Fe^0 particles could be seen for YFAO-1100–0.28 and

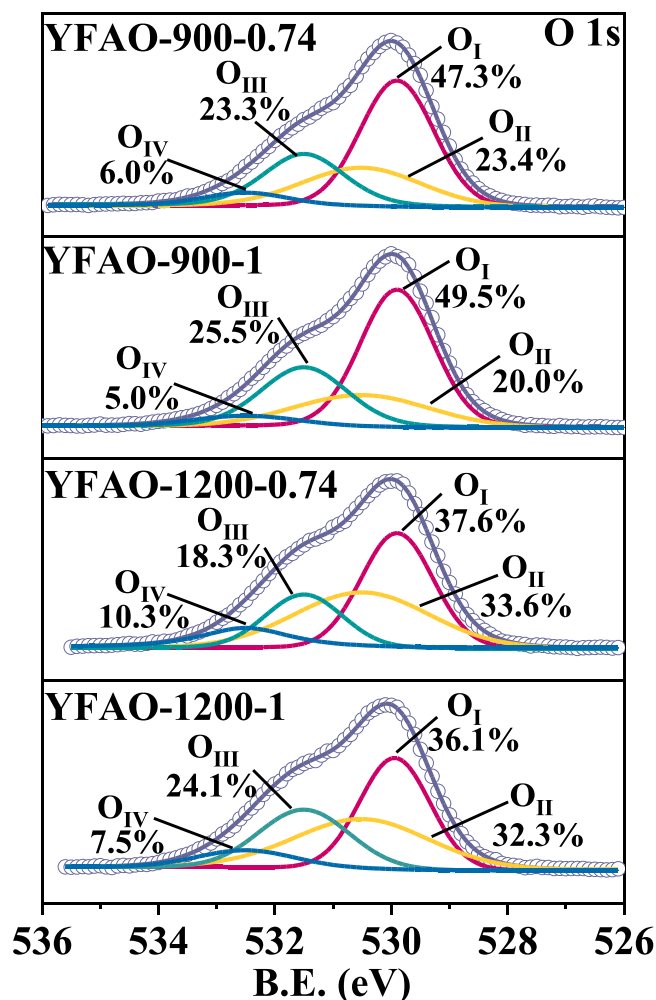


Fig. 10. XPS analysis of the oxygen on the YFAO-T-0.74, YFAO-T-1.

Table 3

XPS analysis of the surface element composition on the YFAO-T-0.74, YFAO-T-1.

Samples	O _{II} /O _I	Surface atomic molar composition (%)				O _{latt} / (Y+Fe+Al)
	O _{ads} / O _{latt}	Y	Fe	Al	O	
YFAO-900-0.74	0.49	16.25	5.36	14.46	63.93	0.84
YFAO-900-1	0.41	16.72	3.90	14.65	64.73	0.91
YFAO-1200-0.74	0.89	16.69	3.54	14.89	64.88	0.69
YFAO-1200-1	0.90	17.20	2.81	15.14	64.85	0.66

YFAO-1200-0.28 (Fig. S13), suggesting that the particle size of Fe⁰ after the beginning of reduction for the sample calcined at lower temperature should be smaller than that at relatively higher temperature. Because Fe⁰ with quite small particle size was difficult to be found out in YFAO-900-0.28 and YFAO-1000-0.28, HRTEM results of only YFAO-1100-0.28 and YFAO-1200-0.28 were shown in which the encapsulation of Fe⁰ sites by garnets could be observed for these two samples (Fig. 8), indicating that Fe⁰ particles might be covered by garnets in the initial of reduction independent on calcination temperature. In order to confirm it, CH₄-TPSR of YFAO-T-0.28 was conducted and the results presented that H₂ and CO concurrently formed for YFAO-T-0.28 except YFAO-1200-0.28 with only H₂ detected at around 600 °C (Fig. S14), pointing toward that Fe⁰ sites was completely encapsulated

by garnets for YFAO-900-0.28, YFAO-1000-0.28 and YFAO-1100-0.28 while partially for YFAO-1200-0.28 with the encapsulation degree of around 19% (Table 2). Combining with the characterization results of YFAO-T-1 (Figs. 6 and 7), we envisioned that the encapsulation of Fe⁰ by garnets was progressively destroyed leading to naked Fe⁰ alongside the reduction for YFAO-T calcined at relatively low temperature while the encapsulation degree became higher with extended reduction for that calcined at high temperature. Then, the characterization of samples after mid-term reduction (YFAO-T-0.74) was performed to verify it. ⁵⁷Fe Mössbauer spectra indicated that the amount of oxygen converted calculated based on Fe⁰ content was similar to that during reaction (0.74 mmol/g) (Table S3) and particle size of Fe⁰ decreased with the increase in calcination temperature (Fig. S15, S16 and Table S3), which was consistent with the results for YFAO-T-1 in terms of variation of particle size (Fig. 4, 5 and Table 1). The encapsulation of Fe⁰ was observed for all the YFAO-T-0.74 (Fig. 9) and only H₂ formed at about 600 °C in CH₄-TPSR (Fig. S17), indicating that Fe⁰ particles was partially covered for YFAO-T-0.74 samples and the encapsulation degree also increased with the calcination temperature (Table 2) in line with that during the late stage of reduction (YFAO-T-1). Combined with the characterization results of YFAO-T-0.28, YFAO-T-0.74 and YFAO-T-1 (Figs. 6, 8 and 9, and Table 2), it could be concluded that the calcination temperature affected the encapsulation degree, and the encapsulation of Fe⁰ sites by garnet was destroyed leading to gradual bareness of Fe⁰ with the extended reduction for YFAO-T calcined at low temperature whereas the encapsulation degree became more and more larger for those calcined at high temperature. Such the distinct encapsulation degree should be responsible for the improved anti-coke of YFAO-T redox catalysts for CLPOM (Figs. 1 and 2).

3.4. Discussion

The results in the present work indicated that anti-coke of YFAO-T OCs for CLPOM was remarkably promoted by the increase in the calcination temperature with high CH₄ conversion and CO selectivity, and the calcination temperature led to the decrease in the oxygen mobility and distinct encapsulation degree of Fe⁰ active sites. In the following section, the effect of oxygen mobility on the encapsulation and its correlation with performance of YFAO-T OCs would be revealed.

3.4.1. Influence of oxygen mobility on the encapsulation of Fe⁰

It was considered that encapsulation state formed as a result of high-temperature H₂ treatment of reducible oxide-supported metals, which caused a reduction of the oxide support with substoichiometric oxygen concentrations and oxide migration on top of the metal nanoparticles [44]. Our results showed that oxygen mobility significantly decreased with the calcination temperature (Fig. 3), which might lead to more oxygen-deficiency on the surface favorable for the encapsulation of Fe⁰ sites. In order to verify it, XPS characterization of YFAO-T-0.74 and YFAO-T-1 was carried out to determine oxygen vacancy on the surface. By deconvoluting the O 1s spectra of Fig. 10, four peaks at 529.8 eV, 530.5 eV, 531.8 eV, 532.8 eV could be attributed to lattice oxygen (O_{latt}), O₂²⁻/O⁻ closely related to the surface oxygen vacancies (O_{ads}), OH⁻ and CO₃²⁻ species, respectively. It was reported that surface oxygen vacancy could be estimated from the ratio of adsorbed oxygen species to lattice oxygen (O_{ads}/O_{latt}) and lowering the lattice oxygen content on the surface led to higher oxygen vacancy concentration [26,45]. O_{ads}/O_{latt} of OCs calcined at 1200 °C (YFAO-1200-0.74 and YFAO-1200-1) was always larger than that calcined at 900 °C (YFAO-900-0.74 and YFAO-900-1) with decreased O_{latt}/(Y+Fe+Al) (Table 3), confirming that declined oxygen mobility resulted in more surface oxygen-deficiency, which was favorable for the encapsulation of Fe⁰ active sites by garnets. As a result, the encapsulation state could be kept during the whole reduction for YFAO-T calcined at high temperature whereas Fe⁰ was progressively naked with the extended reduction for those calcined at low temperature.

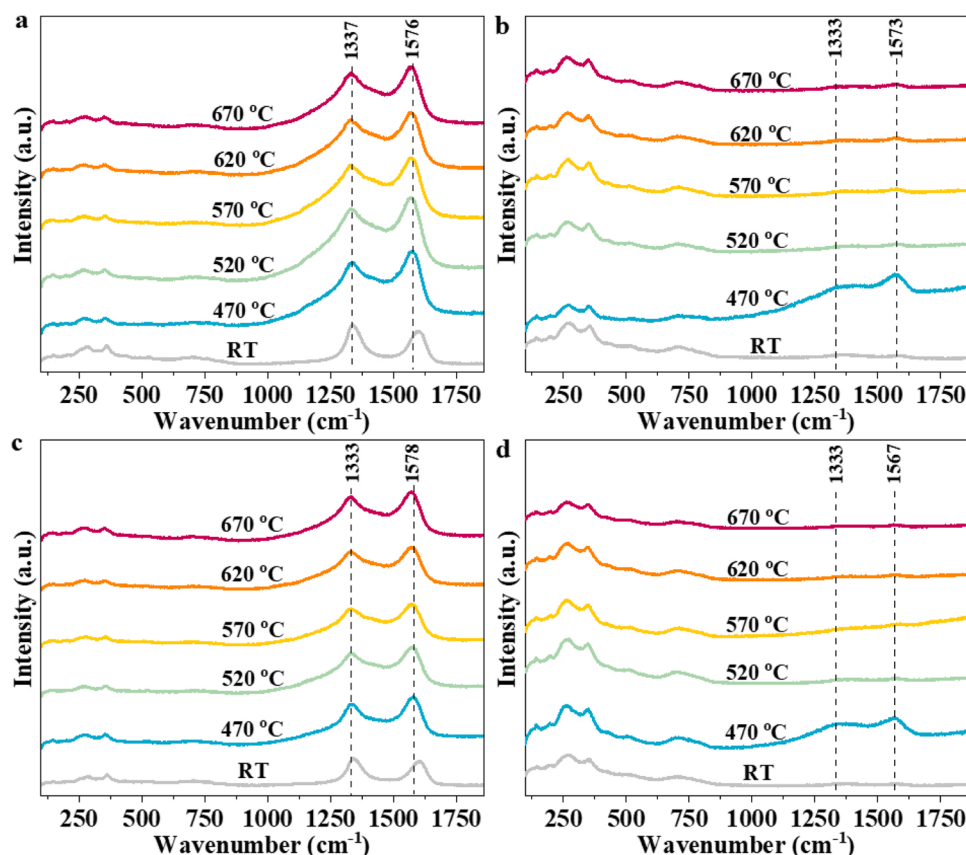


Fig. 11. *In situ* Raman spectroscopy of (a)YFAO-900-0.74, (b)YFAO-1200-0.74, (c)YFAO-900-1, (d)YFAO-1200-1 during CH₄ temperature-programmed reduction.

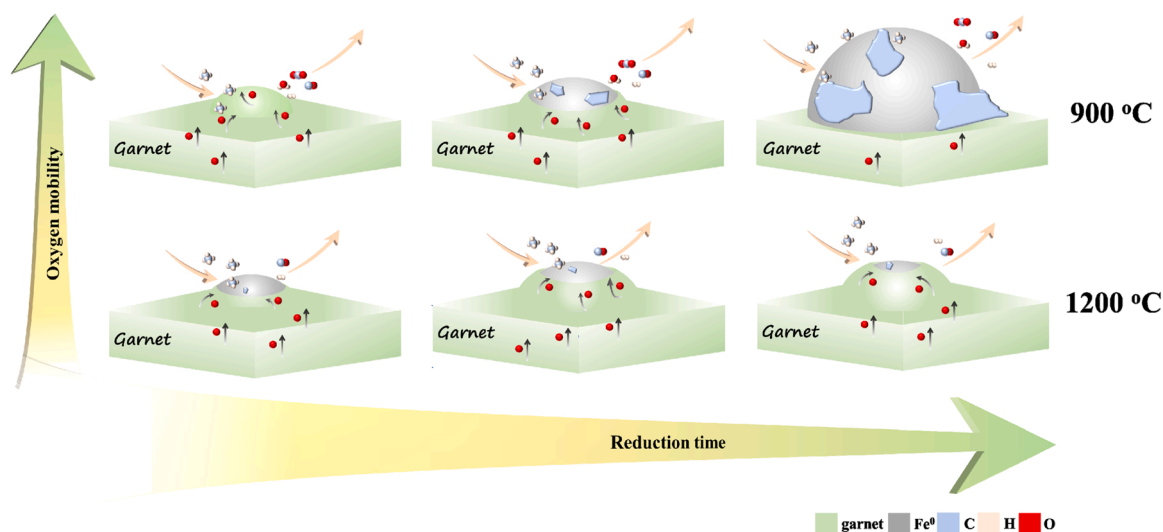


Fig. 12. Reaction model of YFAO-900 and YFAO-1200.

3.4.2. The correlation between encapsulation with performance of YFAO-T

The complete encapsulation of Fe⁰ by CeO₂ and perovskites during preparation and reaction had been reported to improve carbon-resistance of OCs by improving oxygen mobility and avoiding direct contact of CH₄ and Fe⁰. However, the coverage of active sites and insufficient activation of support overlayer for CH₄ usually led to inferior conversion. In the present work, partial encapsulation of Fe⁰ by garnet was for the first time reported and could be maintained during the whole reduction for YFAO-T calcined at higher temperature with relatively small particle size of Fe⁰ (Figs. 6d, 8b, 9d and Table 1), which

not only brought about Fe⁰ active sites for CH₄ activation but also lattice oxygen of garnet shell easier to convert carbon formed to CO compared with YFAO-900 with naked Fe⁰ with large particle size (Fig. 6a). Thus, in-situ Raman spectra of YFAO-900-O and YFAO-1200-O was conducted to study the oxidation of carbon formed by CH₄ decomposition on Fe⁰ sites. For YFAO-900-0.74, the peaks at around 1333 cm⁻¹ and 1576 cm⁻¹ attributed to carbon species were detected at room temperature (Fig. 11a), which was due to coke formation after reduction for 2.1 min with the amount of oxygen converted of 0.74 mmol/g for YFAO-900 (Fig. 1a and S6). Carbon could be always observed whether under

CH₄ or Ar atmosphere with the increase in the temperature (Fig. 11a and S18a), indicating that these carbon species formed on Fe⁰ sites was difficult to be oxidized due to low encapsulation degree of only 4% (Table 2) leading to unavailable lattice oxygen of garnet. In contrast, carbon was observed at 470 °C for YFAO-1200-0.74 because of CH₄ decomposition on Fe⁰ sites and it disappeared with the increase of temperature to 520 °C and did not reappear even to 670 °C (Fig. 11b), which provided strong evidences that the encapsulation of Fe⁰ sites by garnet with higher extent (60% in Table 2) was easier to oxidize carbon formed on Fe⁰ sites. Similar behavior was also observed for YFAO-900-1 with naked Fe⁰ and YFAO-1200-1 with larger encapsulation degree of around 79% (Fig. 11c, d, S18b and Table 2). Consequently, higher encapsulation degree of Fe⁰ by garnets for YFAO-T with lower oxygen mobility not only gave rise to active sites for CH₄ activation but also facilitated the oxidation of carbon species formed on Fe⁰ sites, which was responsible for its superior anti-coke with high CH₄ conversion and CO selectivity, as summarized in Fig. 12. Comparatively, a larger amount of carbon accumulated on naked Fe⁰ for YFAO-T with relatively high oxygen mobility due to inaccessible lattice oxygen of garnet.

4. Conclusions

In summary, the amount of carbon deposition for YFAO-T garnets was prominently decreased by almost 15 times by increasing calcination temperature with CH₄ conversion of about 92%, CO selectivity of nearly 100% and syngas productivity of around 3 mmol/g for CLPOM. It was found that the increase in calcination temperature resulted in the decrease of oxygen mobility thus more surface oxygen vacancy, which influenced the encapsulation of Fe⁰ by garnets. That is, the encapsulation degree of Fe⁰ became larger for YFAO-T calcined at higher temperature during CH₄ reduction while it was progressively destroyed with increase in the reduction extent leading to naked Fe⁰ with large particle size for those calcined at lower temperature. As a result, the encapsulation of Fe⁰ by garnets with the largest degree of around 79% for YFAO-1200 not only brought about Fe⁰ active sites for CH₄ activation but also facilitated the removal of carbon formed by the lattice oxygen of garnet shell to produce CO, which accounted for its superior performance. In contrast, large amount of coke accumulated on sintered and naked Fe⁰ by CH₄ decomposition for YFAO-900 due to inaccessible lattice oxygen of garnets. The present work provided a strategy to improve carbon resistance of Fe-based OCs by tuning strong metal-support interaction (SMSI) based on oxygen mobility for CLPOM.

CRediT authorship contribution statement

Teng Zong: Sample synthesis, Experiment design, Exploration, Data analysis, Writing & editing. **Lin Li:** Experiment equipment. **Yujia Han:** Experiment design, Writing – review & editing. **Chaojie Wang:** Writing – review & editing. **Yu Kang:** Writing – review & editing. **Ming Tian:** Experiment design, Writing & editing. **Chuande Huang:** Writing – review & editing. **Xiaodong Wang:** Supervision, Writing – review & editing.

Declaration of Competing Interest

The authors declare that they have no known competing financial interests or personal relationships that could have appeared to influence the work reported in this paper.

Acknowledgements

The research was supported by the National Natural Science Foundation of China (NSFC) grants (21406225, 21706254 and 22178337). National Key Research and Development Program of China (2016YFA0202-801) and Dalian Institute of Chemical Physics, CAS (DICP I201916).

Appendix A. Supporting information

Supplementary data associated with this article can be found in the online version at doi:10.1016/j.apcatb.2022.121421.

References

- [1] S. Bhavsar, G. Vesar, Chemical looping beyond combustion: production of synthesis gas via chemical looping partial oxidation of methane, *RSC Adv.* 4 (2014) 47254–47267.
- [2] W. Liu, Controlling lattice oxygen activity of oxygen carrier materials by design: a review and perspective, *React. Chem. Eng.* 6 (2021) 1527–1537.
- [3] Y.-Y. Chen, M. Guo, M. Kim, Y. Liu, L. Qin, T.-L. Hsieh, L.-S. Fan, Predictive screening and validation on chemical looping oxygen carrier activation by tuning electronic structures via transition metal dopants, *Chem. Eng. J.* 406 (2021), 126729.
- [4] Z. Cheng, L. Qin, M. Guo, J.A. Fan, D. Xu, L.S. Fan, Methane adsorption and dissociation on iron oxide oxygen carriers: the role of oxygen vacancies, *Phys. Chem. Chem. Phys.* 18 (2016) 16423–16435.
- [5] M. Tang, K. Liu, D.M. Roddick, M. Fan, Enhanced lattice oxygen reactivity over Fe₂O₃/Al₂O₃ redox catalyst for chemical-looping dry (CO₂) reforming of CH₄: Synergistic La-Ce effect, *J. Catal.* 368 (2018) 38–52.
- [6] Y. Liu, L. Qin, J. Pan, Y.-Y. Chen, J.W. Goetze, D. Xu, J.A. Fan, L.-S. Fan, SBA-16-mediated nanoparticles enabling accelerated kinetics in cyclic methane conversion to syngas at low temperatures, *ACS Appl. Energy Mater.* 3 (2020) 9833–9840.
- [7] M. Tang, L. Xu, M. Fan, Progress in oxygen carrier development of methane-based chemical-looping reforming: a review, *Appl. Energy* 151 (2015) 143–156.
- [8] D. Pakhare, J. Spivey, A review of dry (CO₂) reforming of methane over noble metal catalysts, *Chem. Soc. Rev.* 43 (2014) 7813–7837.
- [9] M.S. Fan, A.Z. Abdullah, S. Bhatia, Catalytic technology for carbon dioxide reforming of methane to synthesis gas, *Chemcatchem* 1 (2009) 192–208.
- [10] M.C. Tang, L. Xu, M.H. Fan, Progress in oxygen carrier development of methane-based chemical-looping reforming: a review, *Appl. Energy* 151 (2015) 143–156.
- [11] M. Luo, Y. Yi, S.Z. Wang, Z.L. Wang, M. Du, J.F. Pan, Q. Wang, Review of hydrogen production using chemical-looping technology, *Renew. Sustain. Energy Rev.* 81 (2018) 3186–3214.
- [12] S. Chen, L. Zeng, H. Tian, X. Li, J. Gong, Enhanced lattice oxygen reactivity over Ni-Modified WO₃-based redox catalysts for chemical looping partial oxidation of methane, *ACS Catalysis* 7 (2017) 3548–3559.
- [13] J. Huang, W. Liu, Y. Yang, B. Liu, High-performance Ni-Fe redox catalysts for selective CH₄ to syngas conversion via chemical looping, *ACS Catalysis* 8 (2018) 1748–1756.
- [14] L. Zeng, Z. Cheng, J.A. Fan, L.S. Fan, J.L. Gong, Metal oxide redox chemistry for chemical looping processes, *Nat. Rev. Chem.* 2 (2018) 349–364.
- [15] X. Zhu, Q. Imtiaz, F. Donat, C.R. Müller, F. Li, Chemical looping beyond combustion – a perspective, *Energy Environ. Sci.* 13 (2020) 772–804.
- [16] D. Zeng, Y. Qiu, M. Li, L. Ma, D. Cui, S. Zhang, R. Xiao, Spatially controlled oxygen storage materials improved the syngas selectivity on chemical looping methane conversion, *Appl. Catal. B: Environ.* 281 (2021), 119472.
- [17] L. Huang, M. Tang, M. Fan, H. Cheng, Density functional theory study on the reaction between hematite and methane during chemical looping process, *Appl. Energy* 159 (2015) 132–144.
- [18] D. Li, R. Xu, Z. Gu, X. Zhu, S. Qing, K. Li, Chemical-looping conversion of methane: a review, *Energy Technol.* 8 (2020) 1900925.
- [19] L. Protasova, F. Snijkers, Recent developments in oxygen carrier materials for hydrogen production via chemical looping processes, *Fuel* 181 (2016) 75–93.
- [20] N.L. Galinsky, A. Shafieifarhood, Y.G. Chen, L. Neal, F.X. Li, Effect of support on redox stability of iron oxide for chemical looping conversion of methane, *Appl. Catal. B-Environ.* 164 (2015) 371–379.
- [21] Y. Sun, J. Li, H. Li, Core-shell-like Fe₂O₃/MgO oxygen carriers matched with fluidized bed reactor for chemical looping reforming, *Chem. Eng. J.* (2021), 134173.
- [22] S.Y. Hosseini, M.R. Khosravi-Nikou, A. Shariati, Production of hydrogen and syngas using chemical looping technology via cerium-iron mixed oxides, *Chem. Eng. Process.* 139 (2019) 23–33.
- [23] Y. Liu, H. Liu, X. Wang, X. Ji, J. Wei, J. Zhang, Orthogonal Preparation of SrFeO_{3-δ} nanocomposites as effective oxygen transfer agents for chemical-looping steam methane reforming, *Energy Fuels* 35 (2021) 17848–17860.
- [24] J. Adanez, A. Abad, F. Garcia-Labiano, P. Gayan, L.F. de Diego, Progress in chemical-looping combustion and reforming technologies, *Prog. Energy Combust. Sci.* 38 (2012) 215–282.
- [25] X. Yin, L. Shen, S. Wang, B. Wang, C. Shen, Double adjustment of Co and Sr in LaMnO_{3+δ} perovskite oxygen carriers for chemical looping steam methane reforming, *Appl. Catal. B: Environ.* 301 (2022), 120816.
- [26] X. Zhang, C. Pei, X. Chang, S. Chen, R. Liu, Z.J. Zhao, R. Mu, J. Gong, FeO₆ octahedral distortion activates lattice oxygen in perovskite ferrite for methane partial oxidation coupled with CO₂ splitting, *J. Am. Chem. Soc.* 142 (2020) 11540–11549.
- [27] Y. Kang, M. Tian, C. Huang, J. Lin, B. Hou, X. Pan, L. Li, A.I. Rykov, J. Wang, X. Wang, Improving syngas selectivity of Fe₂O₃/Al₂O₃ with yttrium modification in chemical looping methane conversion, *ACS Catal.* 9 (2019) 8373–8382.
- [28] F. Huang, M. Tian, Y. Zhu, X. Wang, A. Wang, L. Li, J. Lin, J. Wang, Fe-substituted Ba-hexaaluminate with enhanced oxygen mobility for CO₂ capture by chemical looping combustion of methane, *J. Energy Chem.* 29 (2019) 50–57.

- [29] H. Chang, E. Bjørgum, O. Mihai, J. Yang, H.L. Lein, T. Grande, S. Raaen, Y.-A. Zhu, A. Holmen, D. Chen, Effects of oxygen mobility in La-Fe-based perovskites on the catalytic activity and selectivity of methane oxidation, *ACS Catal.* 10 (2020) 3707–3719.
- [30] L. Neal, A. Shafiearhoo, F. Li, Dynamic methane partial oxidation using a Fe₂O₃@La_{0.8}Sr_{0.2}FeO_{3-δ} core-shell redox catalyst in the absence of gaseous oxygen, *ACS Catalysis* 4 (2014) 3560–3569.
- [31] A. Shafiearhoo, N. Galinsky, Y. Huang, Y. Chen, F. Li, Fe₂O₃@La_xSr_{1-x}FeO₃ core-shell redox catalyst for methane partial oxidation, *ChemCatChem* 6 (2014) 790–799.
- [32] X. Yin, S. Wang, R. Sun, S. Jiang, L. Shen, A. Ce-Fe, Oxygen carrier with a core-shell structure for chemical looping steam methane reforming, *Ind. Eng. Chem. Res.* 59 (2020) 9775–9786.
- [33] C. Huang, J. Wu, Y.-T. Chen, M. Tian, A.I. Rykov, B. Hou, J. Lin, C.-R. Chang, X. Pan, J. Wang, A. Wang, X. Wang, In situ encapsulation of iron(0) for solar thermochemical syngas production over iron-based perovskite material, *Commun. Chem.* 1 (2018) 55.
- [34] Y. Kang, Y. Han, M. Tian, C. Huang, C. Wang, J. Lin, B. Hou, Y. Su, L. Li, J. Wang, X. Wang, Promoted methane conversion to syngas over Fe-based garnets via chemical looping, *Appl. Catal. B* 278 (2020).
- [35] Y.Y. Zhu, X.Y. Sun, W.W. Liu, P. Xue, M. Tian, X.D. Wang, X.X. Ma, T. Zhang, Microstructure and reactivity evolution of La-Fe-Al oxygen carrier for syngas production via chemical looping CH₄-CO₂ reforming, *Int. J. Hydrog. Energy* 42 (2017) 30509–30524.
- [36] Z. Yang, Y. Zheng, K. Li, Y. Wang, Y. Wang, H. Wang, Y. Wang, L. Jiang, X. Zhu, Y. Wei, Chemical-looping reforming of methane over La-Mn-Fe-O oxygen carriers: effect of calcination temperature, *Chem. Eng. Sci.* 229 (2021), 116085.
- [37] B. Jiang, L. Li, Q. Zhang, J. Ma, H. Zhang, K. Yu, Z. Bian, X. Zhang, X. Ma, D. Tang, Iron-oxygen covalency in perovskites to dominate syngas yield in chemical looping partial oxidation, *J. Mater. Chem. A* 9 (2021) 13008–13018.
- [38] J. Yang, E. Bjørgum, H. Chang, K.-K. Zhu, Z.-J. Sui, X.-G. Zhou, A. Holmen, Y.-A. Zhu, D. Chen, On the ensemble requirement of fully selective chemical looping methane partial oxidation over La-Fe-based perovskites, *Appl. Catal. B Environ.* 301 (2022), 120788.
- [39] Y. Han, M. Tian, C. Wang, Y. Kang, L. Kang, Y. Su, C. Huang, T. Zong, J. Lin, B. Hou, X. Pan, X. Wang, Highly active and anticoke Ni/CeO₂ with ultralow Ni loading in chemical looping dry reforming via the strong metal-support interaction, *ACS Sustain. Chem. Eng.* (2021).
- [40] Y. Xiao, K. Xie, Active exsolved metal-oxide interfaces in porous single-crystalline ceria monoliths for efficient and durable CH₄/CO₂ reforming, *Angew. Chem. Int. Ed.*, N./a (2021).
- [41] K. Kousi, D. Neagu, L. Bekris, E.I. Papaioannou, I.S. Metcalfe, Endogenous nanoparticles strain perovskite host lattice providing oxygen capacity and driving oxygen exchange and CH₄ conversion to syngas, *Angew. Chem. Int. Ed.* 59 (2020) 2510–2519.
- [42] L. Lindenthal, J. Popovic, R. Rameshan, J. Huber, F. Schrenk, T. Ruh, A. Nenning, S. Löffler, A.K. Opitz, C. Rameshan, Novel perovskite catalysts for CO₂ utilization - Exsolution enhanced reverse water-gas shift activity, *Appl. Catal. B Environ.* 292 (2021), 120183.
- [43] X. Sui, L. Zhang, J. Li, K. Doyle-Davis, R. Li, Z. Wang, X. Sun, Advanced support materials and interactions for atomically dispersed noble-metal catalysts: from support effects to design strategy, *Adv. Energy Mater.* (2021) 2102556.
- [44] J.C. Matsubu, S. Zhang, L. DeRita, N.S. Marinkovic, J.G. Chen, G.W. Graham, X. Pan, P. Christopher, Adsorbate-mediated strong metal-support interactions in oxide-supported Rh catalysts, *Nat. Chem.* 9 (2017) 120–127.
- [45] J. Hu, X. Tang, Q. Dai, Z. Liu, H. Zhang, A. Zheng, Z. Yuan, X. Li, Layered double hydroxide membrane with high hydroxide conductivity and ion selectivity for energy storage device, *Nat. Commun.* 12 (2021) 3409.